A scalable monitoring framework for leaf area index and green area index using 30°-tilted cameras

*Chongya Jiang[1,2,3], *Kaiyu Guan[1,2,3,4], Hongliang Fang[5,6], Youngryel Ryu[7], Kaiyuan Li[1,2]

[1] Agroecosystem Sustainability Center, Institute for Sustainability, Energy, and Environment, University of Illinois at Urbana-Champaign, Urbana, IL 61801, USA

[2] Department of Natural Resources and Environmental Sciences, College of Agricultural, Consumer & Environmental Sciences, University of Illinois at Urbana-Champaign, Urbana, IL 61801, USA

[3] DOE Center for Advanced Bioenergy and Bioproducts Innovation, University of Illinois at Urbana-Champaign, Urbana, IL 61801, USA

[4] National Center for Supercomputing Applications, University of Illinois at Urbana-Champaign, Urbana, IL 61801, USA

[5] LREIS, Institute of Geographic Sciences and Natural Resources Research, Chinese Academy of Sciences, Beijing, 100101, China

[6] College of Resources and Environment, University of Chinese Academy of Sciences, Beijing, 100049, China

[7] Department of Landscape Architecture and Rural Systems Engineering, College of Agriculture and Life Sciences, Seoul National University, South Korea

Summary

- Leaf area index (LAI) and green area index (GAI) are fundamental plant traits. However, there is a lack of ground observation network for LAI/GAI due to technical limitations. Here we present a new method to achieve continuous LAI/GAI monitoring using ordinary cameras.
- By tilting ordinary cameras by 30°, images can cover a large view zenith angle range to measure multi-angular gap fractions and thus to quantify LAI using radiative transfer theory. In addition, using cameras can separate green tissues from non-green tissues. We conducted intensive experiments to evaluate the performance of 30°-tilted cameras and built a countywide LAI/GAI ground observation network.
- LAI/GAI derived from 30°-tilted cameras are consistent with LAI-2200 and destructive samplings. The countywide LAI/GAI ground observation network can capture distinct seasonality of corn, soybean, miscanthus, switchgrass, restored prairie and deciduous forest.
- 30°-tilted cameras provide an accurate, robust, automatic, standardized and scalable method to acquire spatially-distributed and temporally-continuous LAI/GAI at low cost. It is promising for building a LAI ground observation network at regional and global scales.

Introduction

Spatially-distributed and temporally-continuous leaf area index (LAI) data are critical to ecosystem studies. LAI, defined as one half of the total leaf area per unit ground area (GCOS, 2016), is a fundamental plant trait which determines key biophysical processes such as radiative transfer, energy balance and mass exchange of terrestrial ecosystems (Sellers et al., 1995), and therefore it has been selected as an essential climate variable (ECV) by the Global Climate Observing System (GCOS) (GCOS, 2016). However, unlike many other terrestrial ecosystem ECVs, such as fraction of absorbed photosynthetically active radiation (FPAR) (Li and Fang, 2015), albedo (Cescatti et al., 2012), land surface temperature (Li et al., 2021a), soil moisture (Dorigo et al., 2011), and evapotranspiration (Baldocchi, 2019), no infrastructural baseline network exists to provide spatially-distributed and temporally-continuous LAI ground measurements at regional to global scales.

An accurate, robust, automatic, standardized and scalable method is the prerequisite for establishing a ground observation network. LAI is usually quantified by inverting the Beer's Law from gap fraction measurements (Monsi and Saeki, 1953, 2005; Chen et al., 1997; Yan et al., 2019). Four types of field-installed instruments have been used to continuously monitor LAI: hemispherical quantum sensors (Turner et al., 2002; Qu et al., 2014; Ryu et al., 2014), directional (57.5°) quantum sensors (Lecerf et al., 2010; Fang et al., 2018; Brede et al., 2018), hemispherical (fisheye) cameras (Brown et al., 2020; Niu et al., 2021; Banan et al., 2018), and directional (0° or 57.5°) cameras (Ryu et al., 2012, 2014; Baret et al., 2010). Overall, quantum sensors are more convenient to use, while cameras are superior in that (Chen et al., 1997; Yan et al., 2019): (1) images are relatively tolerant to multi-scattering because even bright leaves are identifiable for gap fraction measurements; and (2) images carry more detailed canopy information than light intensity, such as clumping and color. The two types of cameras have their advantages and disadvantages (Yan et al., 2019). Hemispherical cameras can utilize multi-angular gap fractions to constrain radiative transfer models and thus accurate and robust. However, they only use a portion of sensor frames, have substantially-decreased resolution from center to edge, and suffer from the vignetting effect, resulting in more difficult image acquisition and more complex image processing that could limit the scalability for large-scale networks. Directional cameras are less sensitive to camera settings, easier to process thanks to their full-frame usage, small geometric distortion, constant and fine resolution, and homogeneous light distribution within small field of view (FOV). However, existing methods with directional cameras do not provide multi-angular gap fractions to constrain radiative transfer models as hemispherical cameras do. Even with certain camera FOVs, gap fractions derived from directional cameras are simply considered as values of a single view zenith angle (VZA), either 0° or 57.5°.

A major uncertainty for camera-based methods is image classification (Wagner and Hagemeier, 2006). Image classification is challenging because image color varies with many factors such as illumination condition, camera filter, exposure, sensitivity, white balance and chromatic aberration. To date, supervised classification is still commonly used, either by thresholding for a certain color channel (Leblanc et al., 2005), selecting vegetation and background colors (Li et al., 2021b), or defining area of interest from images (Wei et al., 2020). Supervised classification usually needs to be conducted interactively and iteratively (Demarez et al., 2008), which is fairly tedious and time-consuming. Furthermore, supervised classification is subjective and thus prone to uncertainty due to different operators (Fang et al., 2014). Many unsupervised classification algorithms have been developed (Rosin, 2001; Otsu, 1979; Ridler and Calvard, 1978; Macfarlane, 2011), but most studies focused on a single biome, a single camera, and either upward or downward images. When applying the algorithm to a different environment, the classification performance may decline and the error could propagate to LAI quantification (Fang et al., 2018). These limitations prevent camera-based methods from large-spatiotemporal-scale applications.

Photosynthesis and transpiration are mostly active on green tissues rather than non-green tissues. Green area index (GAI), which is defined as the product of green fraction and LAI (Fang et al., 2019; Baret et al., 2010), is therefore more relevant in ecosystem studies than LAI (Gitelson and Gamon, 2015). GAI is traditionally measured by manually counting green tissues instead of whole plants, whereas widely used quantum sensor based optical instruments are unable to measure it. Some studies have used downward viewing cameras to measure GAI by identifying green tissues from images (Li et al., 2021b; Baret et al., 2010). However, such methods are preferred for short and sparse canopies so that the whole plants can be clearly seen and easily classified into green and non-green pixels from downward viewing images. This limitation prevents broad application of cameras for monitoring LAI and GAI.

This study presents a new method to monitor LAI and GAI using 30°-tilted cameras and builds a countywide ground observation network. The rationale is that for an ordinary camera with a certain FOV, titling it leads to a much larger VZA range than pointing towards the zenith (Qu et al., 2021). Therefore, if the VZA values of individual pixels are known, tilted directional cameras can acquire multi-angular gap fractions as hemispherical cameras do. Here the way we use directional cameras is fundamentally different from acquiring single-angular gap fraction, either 0° or 57.5° (Baret et al., 2010; Macfarlane et al., 2007). The usage of directional cameras also avoids the disadvantages of hemispherical cameras, and therefore more practical for building regional and global ground observation networks. We prove the feasibility of the tilted cameras on building a LAI/GAI ground observation network by (1) presenting a generic and fully-automated image processing algorithm for the LAI/GAI quantification from 30°-tilted cameras for both upward and downward viewing cameras as a scalable solution, and (2) conducting comprehensive evaluation over three years using a point-and-shoot camera, a smartphone camera, and 52 time-lapse field cameras in six species at ten sites to demonstrate its scalability (Fig. 1). We envision 30°-tilted cameras can advance the establishment of an infrastructural baseline network for continuous LAI/GAI ground measurements.

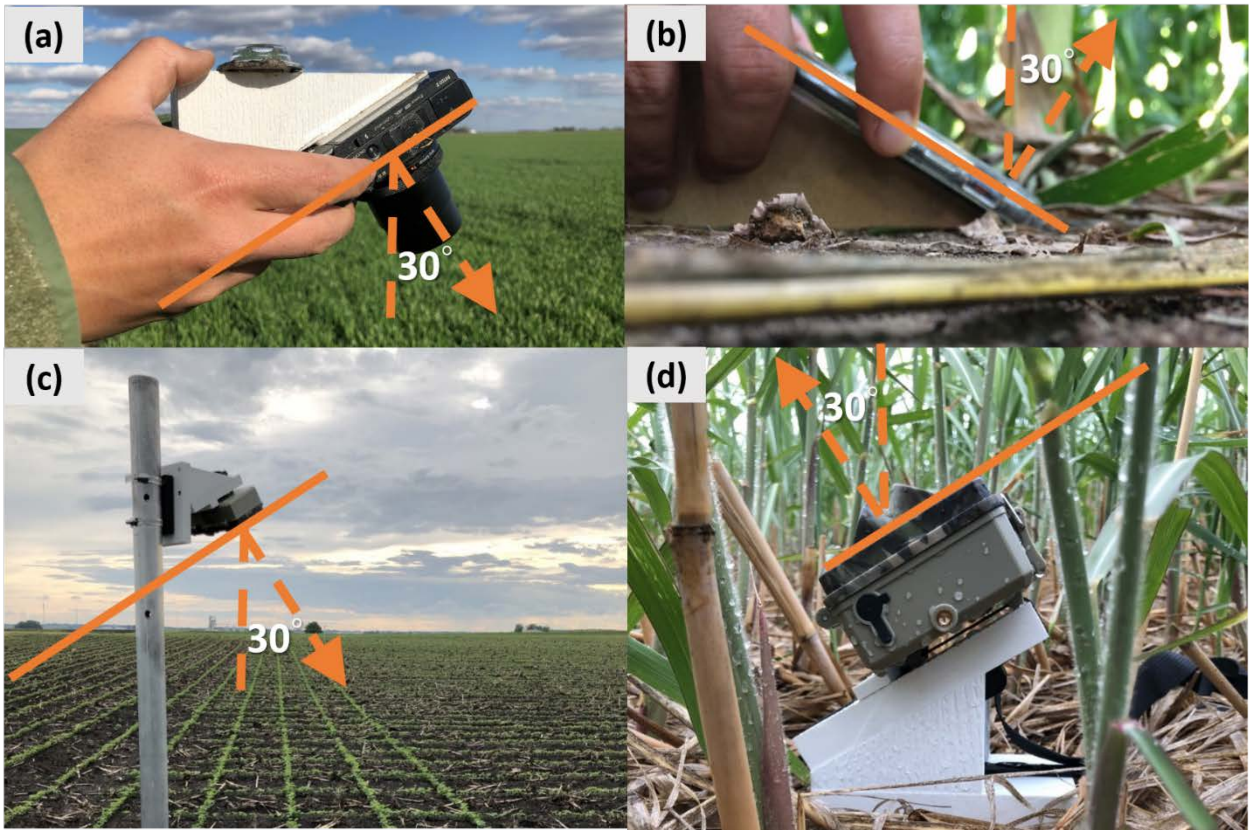

Fig. 1 30°-tilted cameras. (a) A hand-held downward viewing Sony DSC-RX100M5A point-and-shoot camera. (b) A hand-held upward viewing iPhone 8 smartphone rear camera. (c) A field-installed downward viewing Meidase SL122 Pro time-lapse camera. (d) A field-installed upward viewing Meidase SL122 Pro time-lapse camera.

Materials and Methods

Radiative transfer theory and LAI-2200 implementation

Optical methods for LAI ground measurements are built upon the Beer-Lambert Law (Monsi and Saeki, 1953, 2005). Assuming plant leaves are randomly distributed and black, the attenuation of beam light by vegetation canopy in a specific direction is given by (Nilson, 1971):

$$P_0(\theta) = e^{-k(\theta)L} = e^{-\frac{G(\theta)L}{\cos\theta}} \qquad \text{Eqn 1}$$

where $P_0(\theta)$ is the probability that the light has 0 contact with the vegetation canopy, i.e., gap fraction, at the VZA θ, $k(\theta)$ is the light extinction coefficient, $G(\theta)$ is the ratio of the projected leaf area on a plane perpendicular to the view direction to the leaf area which is a function of leaf angle distribution and observation geometry, and L is LAI. Reforming Eqn 1 gives

$$L = -\frac{\cos\theta}{G(\theta)} \ln P_0(\theta) \qquad \text{Eqn 2}$$

Since plant leaves are non-randomly distributed in reality, L in Eqn 2 is effective LAI (L_e) instead of true LAI (L_t). By dividing the space into many small areas and assuming plant leaves are randomly distributed at this small scale but non-randomly distributed at larger scales, whereas $G(\theta)$ is assumed independent of scale, for a given small area j, its L in Eqn 2 is true LAI, and consequently the true LAI of the entire space can be averaged over all small areas (Lang and Xiang, 1986; Fang, 2021; Ryu et al., 2010):

$$L_t = \overline{L_{t,J}} = \overline{-\frac{\cos\theta}{G(\theta)} \ln P_{0,J}(\theta)} = -\frac{cos\,\theta}{G(\theta)} \overline{ln\, P_{0,J}(\theta)} \qquad \text{Eqn 3}$$

To calculate L_e and L_t using Eqn 2 and 3, respectively, $P_0(\theta)$ is easily observed but $G(\theta)$ is hard to acquire. A theorem has been proposed to approximate LAI from multi-angular gap fractions without a prior knowledge of $G(\theta)$ (Miller, 1967; Ryu et al., 2010; Fang, 2021):

$$L_t = 2\int_0^{\pi/2} -\overline{\ln P_{0,J}(\theta)} \cos\theta \sin\theta \, d\theta \qquad \text{Eqn 4}$$

LAI-2200 Plant Canopy Analyzer (the follow-up to LAI-2000; LI-COR Inc., Lincoln, USA) is a widely-used standard commercial optical instrument (Welles and Norman, 1991; Yan et al., 2019). LAI-2200 equips a fisheye lens and five quantum sensors to measure the interception of blue light at five VZA rings (0–12.3°, 16.7–28.6°, 32.4–43.4°, 47.3–58.1°, and 62.3–74.1°) from readings taken above (A) and below (B) the canopy (LI-COR, 2021), and gap fractions are subsequently calculated by:

$$P_{ij} = \frac{B_{ij}}{A_{ij}} \qquad \text{Eqn 5}$$

where i and j refer to the ith VZA rings (i = 1…5) and the jth observation (j = 1…N), respectively. Accordingly, Equ 4 is implemented by:

$$L_t = 2\sum_{i=1}^{n} -\overline{\ln P_{ij}} \cos\theta_i \, W_i \qquad \text{Eqn 6}$$

where W_i is the weight of the ith ring, defined as:

$$W_i = \frac{\sin\theta_i \, d\theta_i}{\sum_{i=1}^{5} \sin\theta_i \, d\theta_i} \qquad \text{Eqn 7}$$

where dθ = 12.2°, 12.2°, 11.8°, 13.2° and 13.2° for the five VZA rings, respectively.

30°-tilted camera implementation

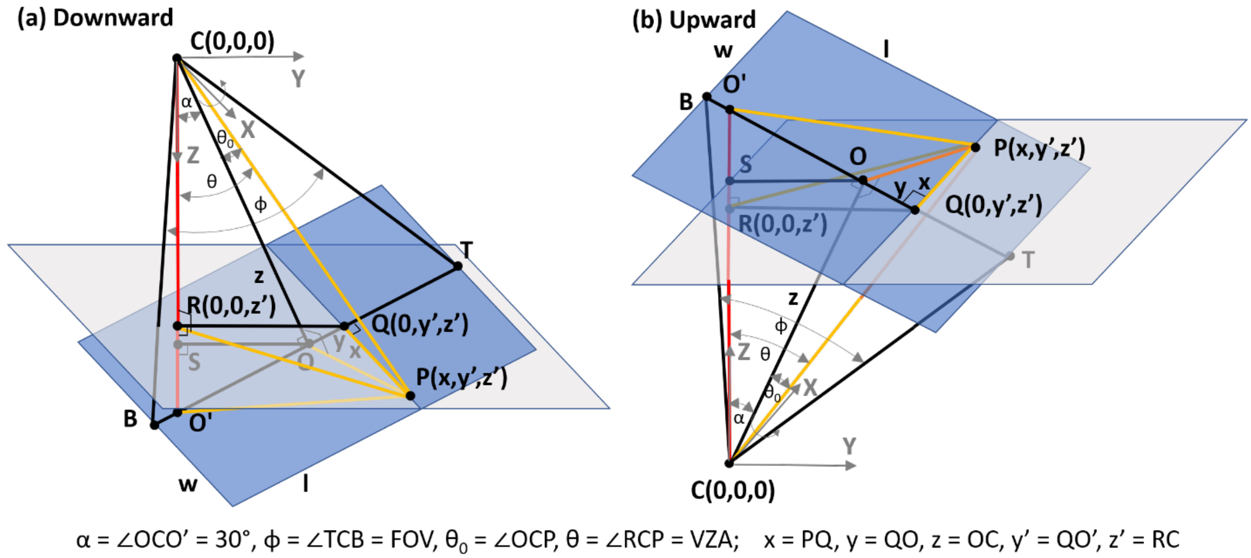

Fig. 2 Geometry of a downward (a) and upward (b) viewing 30°-tilted cameras. X-, Y- and Z-axis are the axis that the camera rotates around, that the camera tilts towards, and the zenith direction, respectively. Red, black, and yellow lines indicate the Z-axis, lines on the Y-Z plane, and lines passing an arbitrary image pixel *P*, respectively. Blue and gray areas indicate the image and the horizontal plane passing the pixel *P*, respectively. *C*: camera. *O*: center of the image. *T*: top center of the image. *B*: bottom center of the image. *O*': intersection of the Z-axis and the image. *Q*: projection of *P* on the Y-Z plane. *R*: projection of *Q* on the Z-axis. *S*: projection of *O* on the Z-axis. (x, y, z) and (x, y', z') are coordinates of P for a non-tilted and a tilted camera, respectively, with C as the origin. l and w are image length and width, respectively. α = 30° is the tiling angle. φ is the vertical (long-side) FOV. θ_0 and θ are VZAs of P for a non-tilted (α = 0°) and a tilted camera, respectively.

If the VZA values of individual pixels are known, cameras can acquire multi-angular observations. As is illustrated in Fig. 2, the VZA of an arbitrary image pixel *P* of a α-degree-tilted camera can be calculated as:

$$\cos\theta = \frac{RC}{PC} = \frac{SC - SR}{\sqrt{(PQ^2 + QO^2 + OC^2)}} = \frac{z\cos\alpha - y\sin\alpha}{\sqrt{x^2 + y^2 + z^2}} \qquad \text{Eqn 8}$$

where x = column number of the pixel P - $w/2$, $y = l/2$ - row number of the pixel P, and $z = (l/2) / [\tan(\varphi/2)]$.

This theoretical model (Eqn 8) enables the usage of ordinary cameras to mimic the observation geometry of LAI-2200 by tilting the cameras (Fig. 3). For example, an iPhone 8 (Apple Inc., Cupertino, USA) rear camera has a $\varphi \approx 65.5°$, l = 4032 px, and w = 3024 px which are provided in the exchangeable image file format (EXIF) embedded in images, then a non-tilted (α = 0°) camera has a maximum VZA (θ_0) about 38.8°, whereas tilting it by 30° along the vertical (long-side) direction (α = 30°) leads to a maximum VZA (θ) about 64.9°, which fully covers the first four rings of LAI-2200 and part of its fifth ring. Further increase of the tilting angle may lose the opportunity to observe in the zenith direction, which is critical to quantify the fraction of vegetation cover (White et al., 2000). With an α = 45°, iPhone 8 can reach a maximum VZA (θ) of 78.7°, but its minimum VZA (θ) also increases to 12.3°. Therefore, we suggest using 30° to balance the maximum and minimum VZAs.

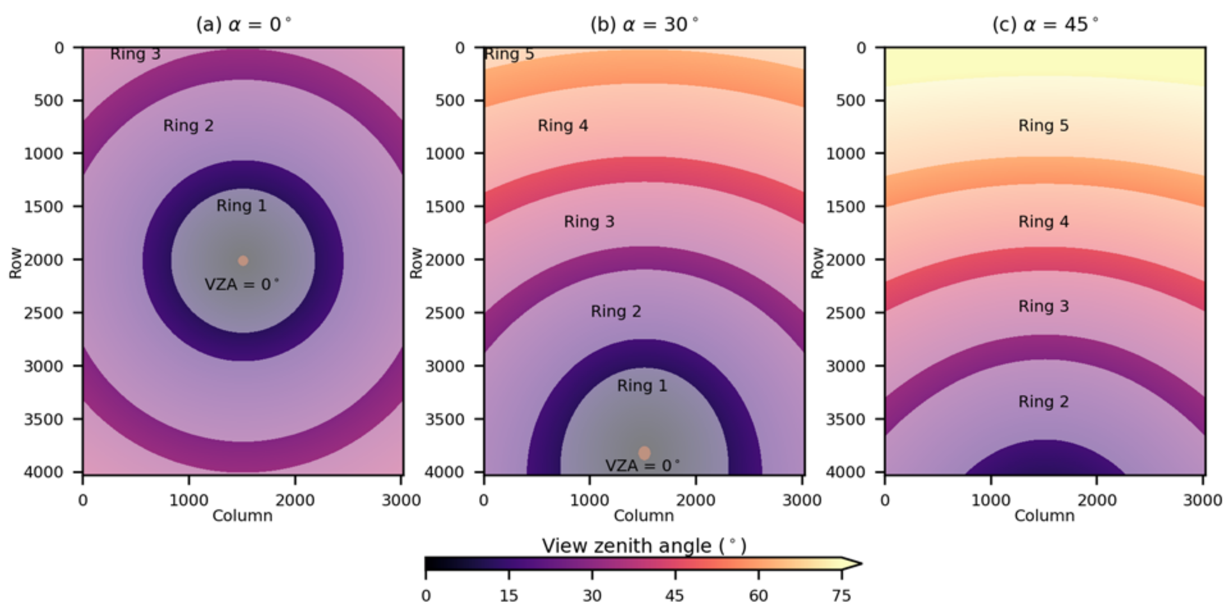

Fig. 3 VZAs of individual pixels by tilting an iPhone 8 rear camera by (a) 0°, (b) 30°, and (c) 45°, calculated using Eqn 8. The five VZA rings corresponding to LAI-2200 are highlighted. The zenith direction is marked by a red circle.

The theoretical model (Eqn 8) is only applicable to ideal cases in which all image projections are linear (Fig. 2). However, in reality, imperfect camera/lens design and fabrication can cause various distortions, and the FOV information provided by the manufacturer can be inaccurate. To assess these impacts on VZA quantification, we conducted a simple in-lab experiment (Fig. 4). According to Fig. 2a, we mounted a 30°-tilted camera in front of a leveled cutting mat. A laser pen was placed on the cutting mat vertically pointing towards the center of the camera lens. The position of the laser pen was therefore the nadir point, and its distance from the center of the camera lens (i.e., camera height) was measured by the laser pen. We used the intersection points of regular grids on the cutting mat as control points, and their distances from the nadir point can be obtained. Subsequently, the VZA values of these control points were calculated by the arctangent function and used as benchmarks.

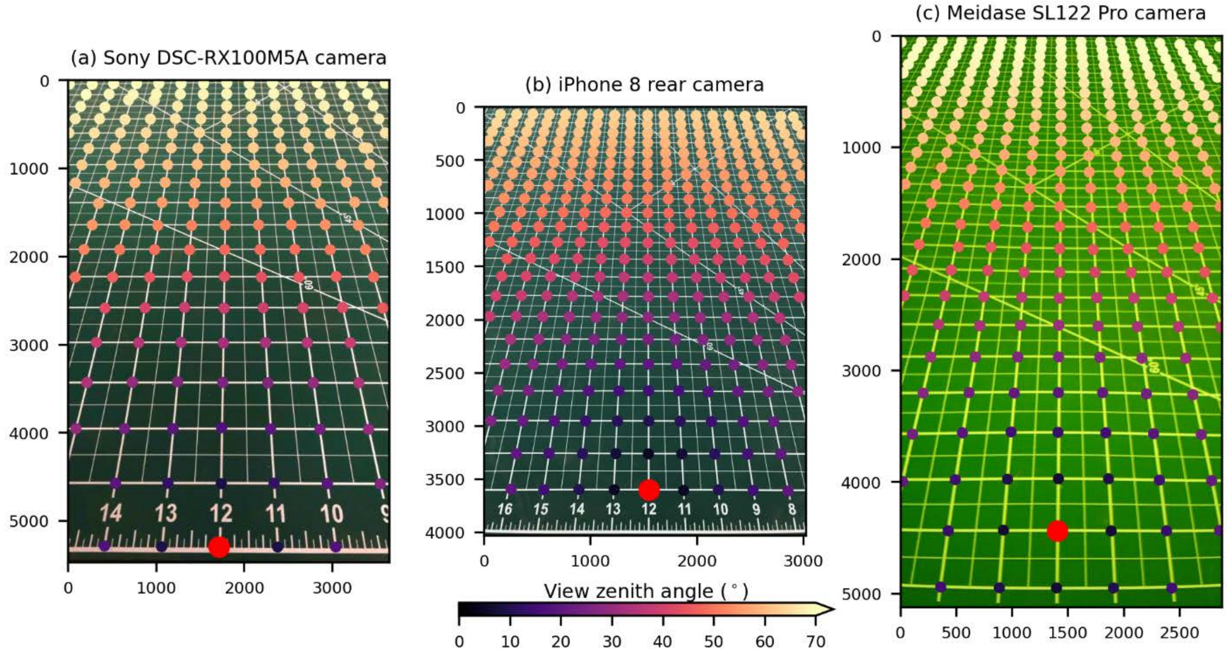

Fig. 4 VZAs of control points for (a) a 30°-tilted Sony DSC-RX100M5A point-and-shoot camera, (b) a 30°-tilted iPhone 8 smartphone rear camera, and (c) a 30°-tilted Meidase SL122 Pro time-lapse field camera. The nadir point is marked by a red circle.

We found that the theoretical model (Eqn 8) well described the distribution of VZA for three different 30°-tilted cameras (Fig. 5). The root mean square error (RMSE) values were less than 4.5° and the relative mean average error (MAE) were less than 7.5%. In particular, iPhone 8 has the lowest geometric error probably because of anti-distortion algorithms applied to nowadays smartphones (Shih et al., 2019). To further improve the VZA quantification, we used these control points to fit an empirical 5th polynomial function (Eqn 9):

$$\begin{aligned}\theta = {} & p_{00} \\ + {} & p_{10}x + p_{01}y \\ + {} & p_{20}x^2 + p_{11}xy + p_{02}y^2 \\ + {} & p_{30}x^3 + p_{21}x^2y + p_{12}xy^2 + p_{03}y^3 \\ + {} & p_{40}x^4 + p_{31}x^3y + p_{22}x^2y^2 + p_{13}xy^3 + p_{04}y^4 \\ + {} & p_{50}x^5 + p_{41}x^4y + p_{32}x^3y^2 + p_{23}x^2y^3 + p_{14}xy^4 + p_{05}y^5\end{aligned} \qquad \text{Eqn 9}$$

where θ, x and y are VZA and image coordinates of a control point, respectively, and p_{ab} (a = 0, …, 5 and b = 0, …, 5) are fitting parameters. By using this calibrated polynomial model, the RMSE values and relative errors were further reduced to <0.5 and <0.5%, respectively (Fig. 8).

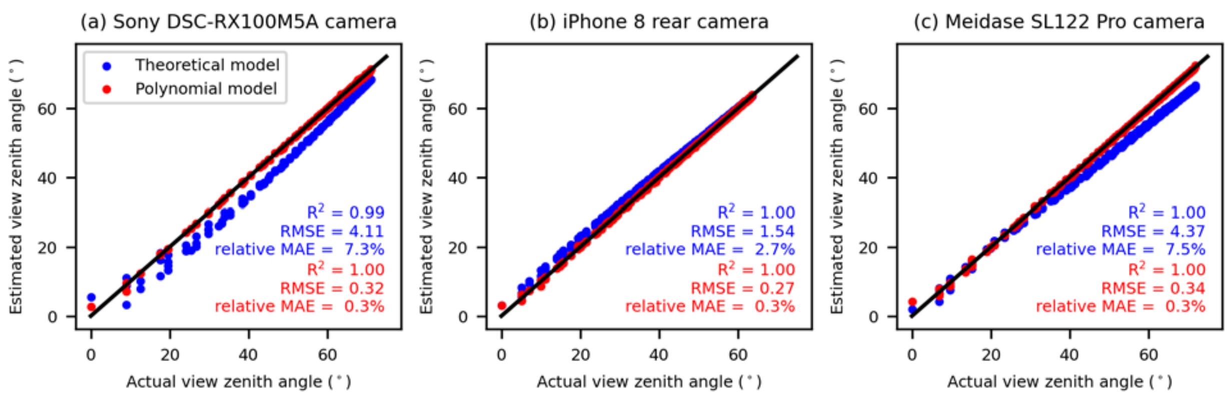

Fig. 5 Comparison between actual and estimated VZAs for (a) a 30°-tilted Sony DSC-RX100M5A point-and-shoot camera, (b) a 30°-tilted iPhone 8 smartphone rear camera, and (c) a 30°-tilted Meidase SL122 Pro time-lapse field camera.

To measure gap fractions within the five VZA rings, per-pixel image classification is needed to identify gaps. Although many automatic image classification algorithms have been presented to separate plant tissues from background (Macfarlane, 2011; Wang et al., 2019), they either work for upward or downward viewing images, but not both. To fill this gap, we proposed to convert RGB images to vegetation index (VI) images on which plant pixels have higher values than background pixels, either sky (upward) or soil (downward). By doing so, generic histogram analysis can be used for thresholding the VI images.

Suitable VIs should enhance the contrast between plant tissues and background while minimizing the within-class differences. For upward viewing images, the blue channel has been widely used because sky is overall bright while vegetation is dark (Leblanc et al., 2005). However, sky brightness could be heterogeneous if sun and clouds are involved. We therefore considered color in addition to brightness: sky is relatively blue while vegetation is green or yellow/brown. Accordingly, the algorithm uses the product of blue channel brightness B and relative blueness B/(R+G+B) as the feature β. For downward viewing images, the algorithm uses the a* channel of the L*a*b* color space as the feature (Schanda, 2007), because the a* channel is relative to the green–red opponent colors and has large contrast between green vegetation and yellow soil (Wang et al., 2019). For both β and a*, vegetation pixels have lower values than background pixels, we therefore defined VI as:

$$VI = 1 - \frac{X - X_{min}}{X_{max} - X_{min}} \qquad \text{Eqn 10}$$

where X refers to β and a* for upward and downward viewing images, respectively, and X_{min} and X_{max} are the minimum and maximum X values of the image, respectively. VI ranges from 0 to 1, with higher values indicating higher probability of being vegetation (Fig. 6 and 7).

From an VI image a histogram can be built, and a threshold can be identified according to the histogram shape. Defining a peak as a VI whose frequency is the highest within a window, the algorithm gradually increases the searching radius until there are no more than two peaks detected (Fig. 6). For each peak, if the mean color is non-blue (G > B or R > B) in upward viewing images, or green (G > R and G > B) in downward viewing images, the peak is treated as vegetation otherwise background. If a background peak and a vegetation peak are detected, then the threshold is the valley between the two peaks (Fig. 6a,b). If two peaks are detected and both are background, then the peak with a larger VI value is considered as the single background peak. If two peaks are detected and both are vegetation, then the peak with a smaller VI value is considered as the single vegetation peak. Subsequently, the algorithm uses the foot of the single peak as the threshold (Fig. 6c,d). Pixels with VI larger than the threshold are classified as vegetation. A morphological processing is finally employed to remove noises. Examples of classification results under different illuminations and crop growth conditions are shown in Fig. 7. All codes are available upon request.

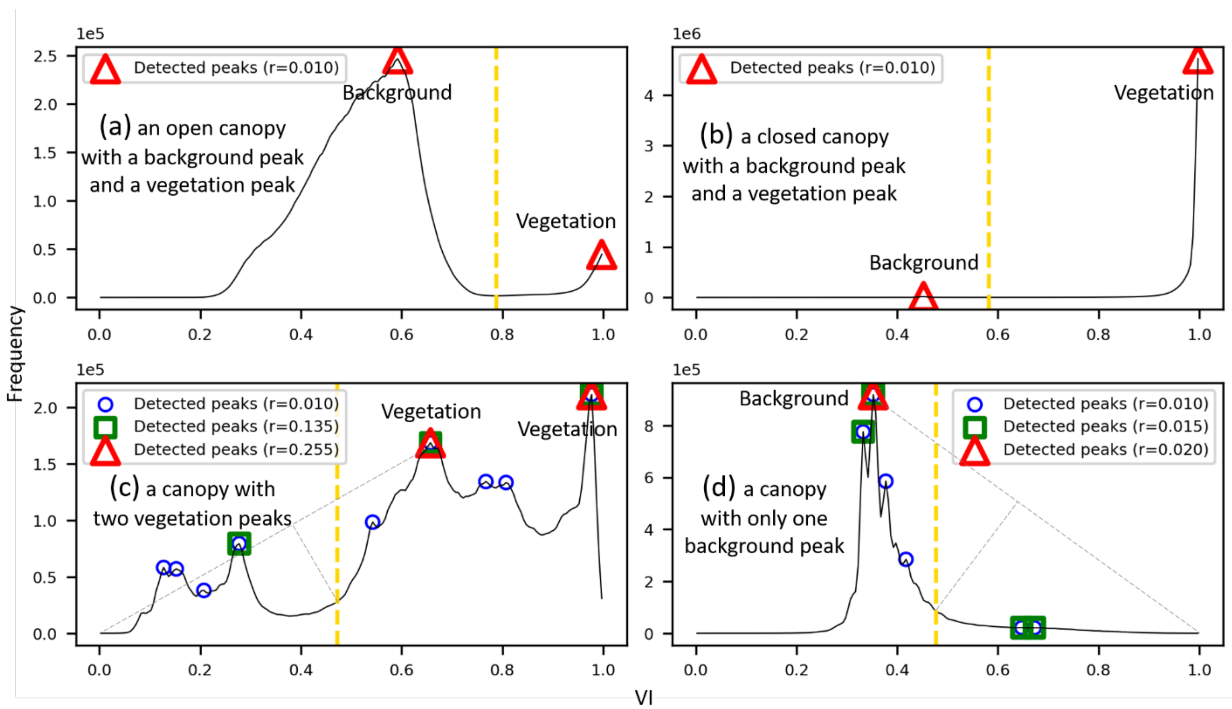

Fig. 6 VI histograms and thresholding. Red: final peak detections. Green and blue: intermediate peak detections. Parentheses: searching radius for peak detections. Gray: ancillary lines for foot detection. Gold: resultant thresholds.

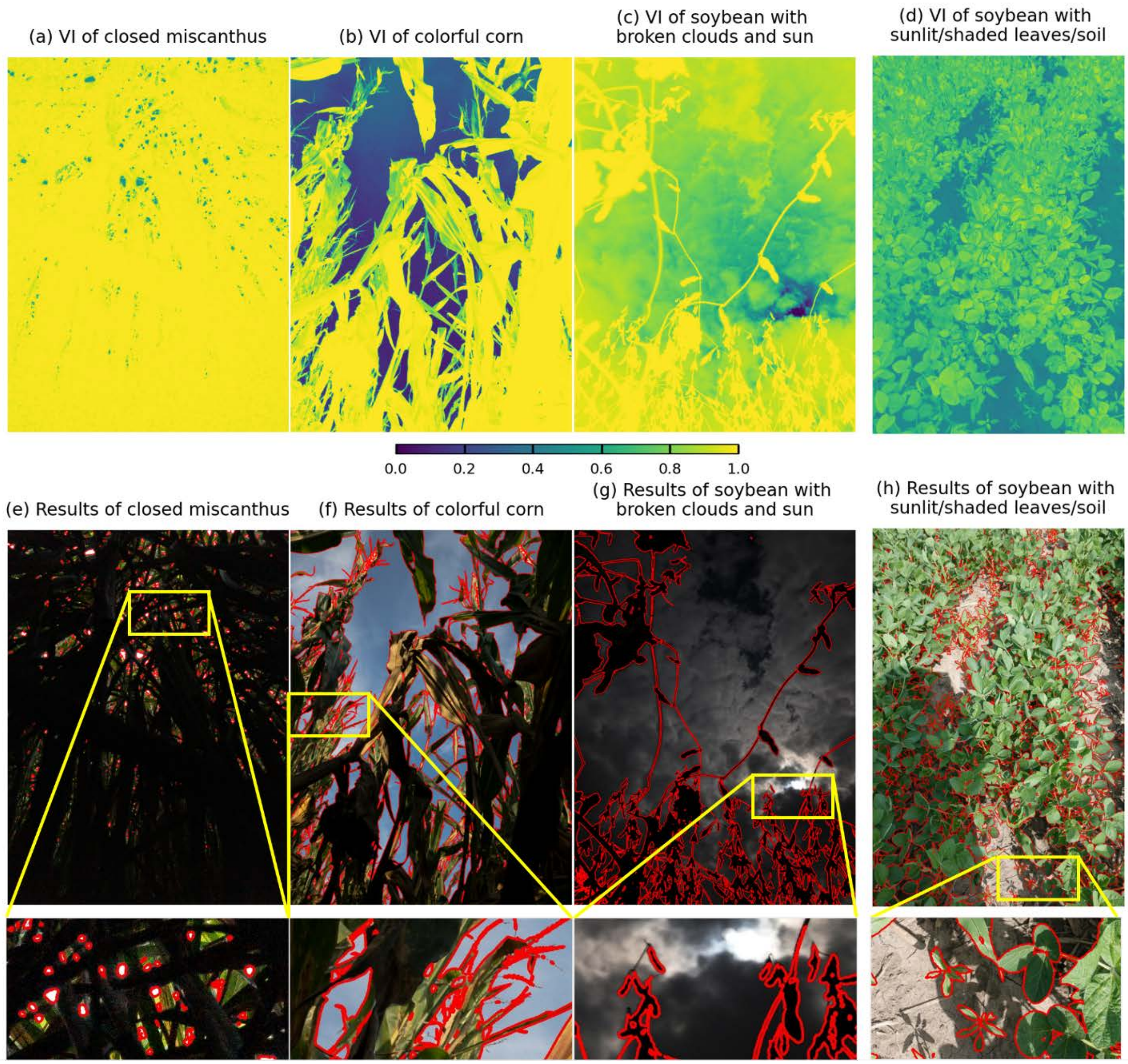

Fig. 7 Automatic image classification to separate vegetation from background under different condition. Upper panel: VIs. Lower panel: boundaries of the detected plant tissues overlaid on RGB images.

Gap fractions can be calculated from a classified image by:

$$P_{ij} = 1 - \frac{N_{plant,ij}}{N_{total,ij}} \quad \text{Eqn 11}$$

where $N_{plant,ij}$ and $N_{total,ij}$ are the amount of plant pixels and the total amount of pixels in the ith ring on the jth image, respectively. Subsequently, Eqn 6–7 can be used to calculate LAI in same way as LAI-2200.

GAI estimation

Cameras can acquire leaf color information in addition to gap fraction information, which enables the estimation of GAI in addition to LAI. Here we simply consider all red-like (R > G or R > B) plant pixels as yellow/brown tissues, and assume the green fraction observed by the camera is the same as the plants, then GAI L_G can be calculated as:

$$L_G = L_t \frac{N_{green}}{N_{plant}} \quad \text{Eqn 12}$$

where N_{green} and N_{plant} are the amount of green tissue and total plant pixels, respectively.

Field measurements

Table 1. Field measurements in Champaign County, Illinois, USA. ESU: elementary sampling unit.

Year	Site	Plant	ESU	Instrument	Period
2020	US-Bo1	Soybean	16	Sony (downward)	06/26 - 07/15
				iPhone (upward)	07/20 - 10/02
				LAI-2200	06/26 - 10/02
				Scanner	06/15 - 10/02
	Energy Farm	Corn	8	Sony (upward)	06/27 - 07/17
				iPhone (upward)	07/24 - 10/13
				LAI-2200	06/27 - 10/13
	Energy Farm	Miscanthus	8	Sony (upward)	06/27 - 07/17
				iPhone (upward)	07/25 - 11/07
				LAI-2200	06/27 - 11/07
	Energy Farm	Soybean	8	iPhone (upward)	07/26 - 10/06
				LAI-2200	07/26 - 10/06
2021	US-Bo1	Corn	1	Meidase (downward ×1)	06/02 - 06/11
				Meidase (upward ×10)	06/11 - 09/14
				LAI-2200	06/07 - 09/13
	Energy Farm	Soybean	1	Meidase (downward ×1)	06/04 - 07/07
				Meidase (upward ×2)	07/07 - 09/27
				LAI-2200	06/28 - 09/27
				Scanner	05/30 - 09/18

2022	US-Bo1	Soybean	1	Meidase (downward ×1)	05/19 - 10/04
				Meidase (upward ×8)	06/15 - 10/04
	Commercial	Soybean	1	Meidase (downward ×1)	05/19 - 09/29
				Meidase (upward ×8)	06/15 - 09/29
	Energy Farm	Soybean	1	Meidase (upward ×2)	07/13 - 10/01
	Commercial	Corn	1	Meidase (downward ×1)	05/19 - 10/13
				Meidase (upward ×8)	06/15 - 10/13
	Farm of Future	Corn	1	Meidase (downward ×1)	06/21 - 10/16
				Meidase (upward ×8)	06/19 - 10/16
	Farm of Future	Corn	1	Meidase (downward ×1)	06/21 - 10/16
				Meidase (upward ×2)	06/19 - 10/16
	Energy Farm	Miscanthus	1	Meidase (downward ×1)	05/20 - 11/07
				Meidase (upward ×2)	06/03 - 11/07
	Energy Farm	Switchgrass	1	Meidase (downward ×1)	05/20 - 11/03
				Meidase (upward ×2)	06/03 - 11/03
	Energy Farm	Restored prairie	1	Meidase (upward ×2)	06/03 - 11/03
	Busey Woods	Deciduous forest	1	Meidase (upward ×2)	07/19 - 11/14

To evaluate the performance of 30°-tilted cameras, field experiments were conducted during 2020–2022 in Champaign County, Illinois, USA (Table 1). Two hand-held and 12 field-installed cameras were validated by LAI-2200 and destructive samplings in 2020 and 2021, respectively, whereas a network of 52 cameras were built in 2022.

In 2020, two hand-held cameras were used: a Sony DSC-RX100M5A point-and-shoot camera (Sony Inc., Minato, Japan; Fig. 1a) and an iPhone 8 smartphone rear camera (Fig. 1b). Measurements were taken in a corn field, a soybean field, and a miscanthus field at the University of Illinois Energy Research Farm, and also at an AmeriFlux site US-Bo1 with soybean planted. At Energy Farm, eight elementary sampling units (ESUs) were selected in each of the three fields, whereas 16 ESUs were selected at US-Bo1. Downward viewing images were taken at US-Bo1 before July 20, 2020, with 8–20 images taken in different azimuth directions at a height of approximately 1.3 m within each ESU. In other cases, upward viewing images were taken by putting the camera on the ground. Relative exposure was set -2 to avoid overexposure by using an app Lightroom (Adobe Inc., San Jose, USA). To account for the row effect, eight upward viewing images were taken at different positions following the spatial sampling protocol suggested by the LAI-2200 manual (LI-COR, 2021). All measurements were conducted within two hours after sunrise or before sunset, or under cloud conditions during daytime.

In 2021, 12 Meidase SL122 Pro time-lapse field cameras (Meidase Inc., Shenzhen, China) were installed at two fields. In the US-Bo1 corn field, one downward viewing camera (D) mounted on a pole at a height of 1.8 m and ten upward viewing cameras sitting on the ground were deployed in the 10 m × 10 m ESU (Fig. 8), before and after June 11, respectively. The ten upward viewing cameras were split into two groups. One group with eight cameras (A1–A4 and B1–B4) were deployed in the same manner with the spatial sampling protocol suggested by the LAI-2200 manual (LI-COR, 2021). The other group with two cameras (C1 and C2) were deployed in between the row direction and the perpendicular direction, with one camera at a position of ¼ between two rows and the other at a position of ¾ between two rows. In the Energy Farm soybean field, only one downward viewing camera (D) and two upward viewing cameras (C1 and C2) were used within a 10 m × 10 m ESU, before and after July 7, respectively. A customized firmware enabling low exposure was updated to each camera to avoid overexposure. All field cameras were set to take pictures at 30 min intervals, but only one image near sunrise/sunset or under cloud conditions was used each day. Occasionally, the automatic image classification failed to find a reasonable valley/corner from the multi-peak VI histogram because of the chromatic aberration of this low-cost field camera or reduced image quality due to water and dust. In this case, manual selection of histogram valley/corner was applied to the VI image for the image classification.

In 2022, a total of 52 Meidase cameras were installed at ten fields, including three corn fields, three soybean fields, one miscanthus field, one switchgrass field, one restored prairie field, and one deciduous forest field. To account for the row effects for corn and soybean, we used eight upward viewing cameras (A1–A4 and B1–B4) in four fields, and used the combination of A4 and B3 in two fields. For other species without row effects, we simply deployed two upward viewing cameras within the ESU. Data gaps occurred due to water or debris on camera lens, close leaves, water leakage, battery or SD card problems, or unknown outage. We conducted an average bi-weekly site visit to minimize data gaps. For each camera, a temporal interpolation was applied to gap fractions to fill data gaps. Since LAI and GAI were calculated from gap fraction measurements by multiple cameras, they were tolerant to gap fraction gap filling for individual cameras.

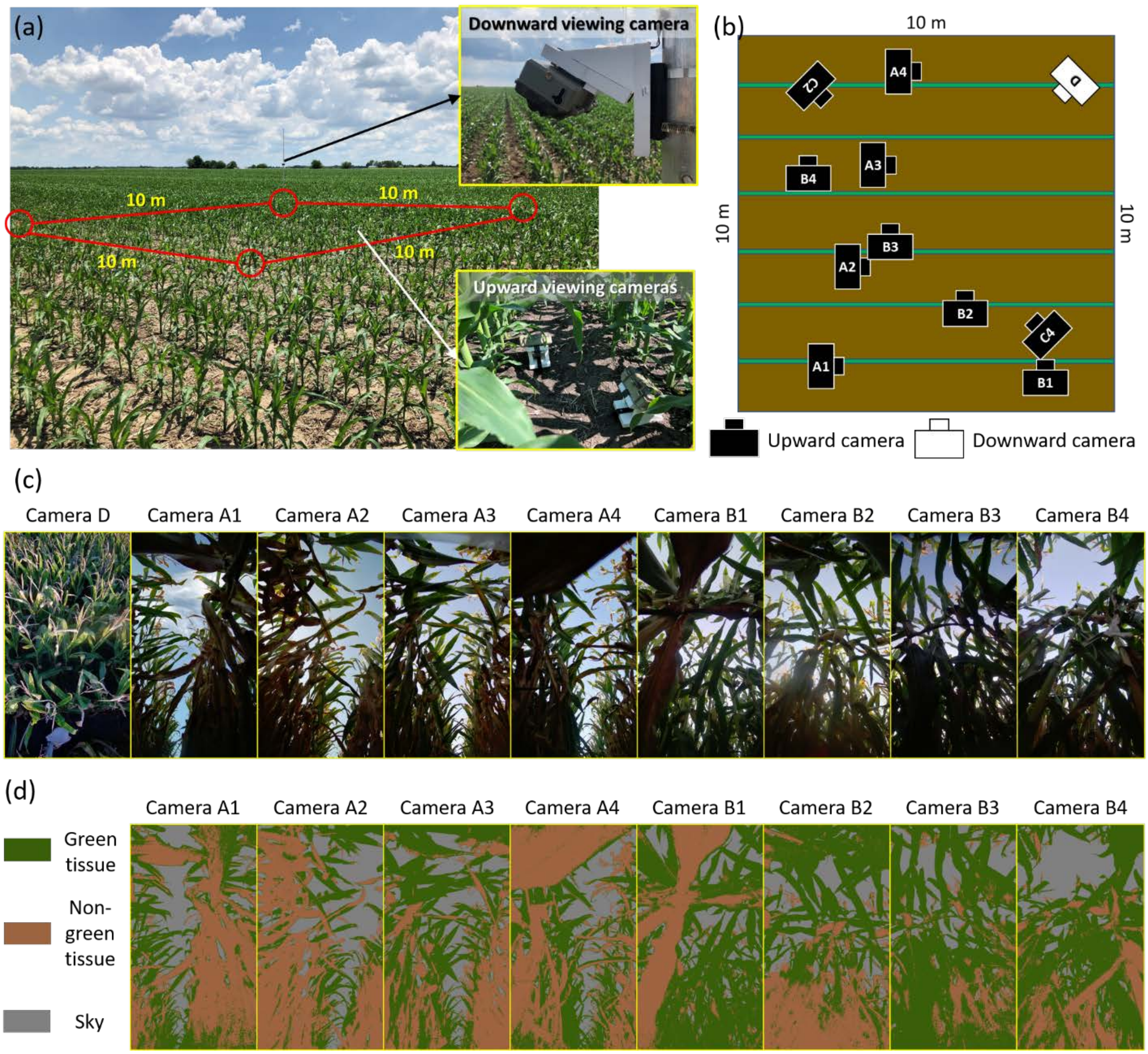

Fig. 8 Deployment of 30°-tilted cameras in the field. (a) An ESU in a corn field. (b) Schematic plot of the camera deployment within the ESU. A: in the direction along rows. B: in the direction perpendicular to rows. C: in the direction in between A and B. 1: at the position in rows. 2: at the position ¼ of the way between the rows. 3: at the position of mid-row. 4: at the position ¾ of the way between the rows. (c) Example images. (d) Classification of example images.

To validate 30°-tilted cameras on LAI quantification, we measured LAI using LAI-2200 in the same ESUs. The time difference between LAI-2200 measurements and hand-held camera measurements were all within two days. All LAI-2200 measurements were conducted within one hour after sunrise or before sunset. The sampling strategy was the same as those of 30°-tilted cameras (A1–B4). A 45°-FOV cap was used to cover the lens in all measurements.

To validate 30°-tilted cameras on GAI quantification, we also conducted destructive sampling at the US-Bo1 and Energy Farm soybean fields in 2020 and 2021, respectively. On each sampling day, 3–8 plants were selected, harvested and measured near the ESUs. Each plant was measured using a portable scanner (Epson Inc., Japan) in the field immediately after harvest. Leaves, stems and beans were separately scanned and their areas were summed up for LAI calculation. Green and non-green tissues proportions were classified for GAI quantification.

Results

Validation for hand-held cameras

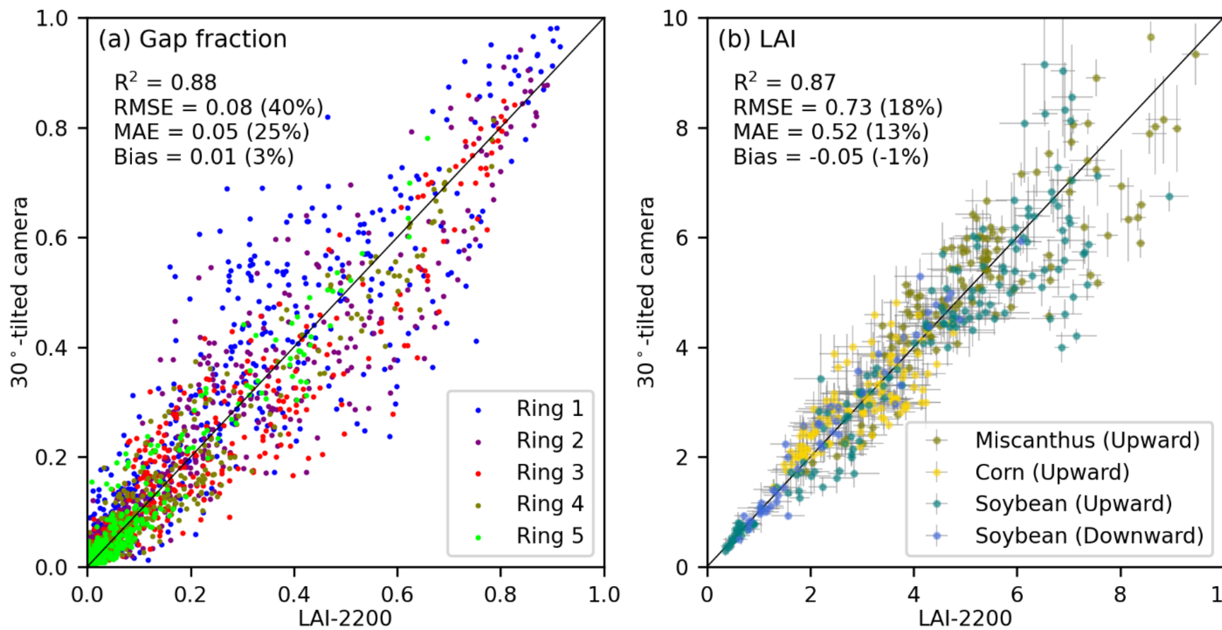

Fig. 9 Comparison of (a) gap fraction and (b) LAI between 30°-tilted hand-held cameras and LAI-2200. Each dot refers to the average value over eight measurements within an ESU.

With the accurate VZA quantification (Fig. 5) and image classification (Fig. 7), gap fractions measured by 30°-tilted cameras are consistent with those measured by LAI-2200 over corn, soybean and miscanthus (Fig. 9a), indicated by a low RMSE (0.08), a low relative MAE (25%), and a small bias (0.01). The largest error is from the first VZA ring (0–12.3°), with a RMSE of 0.12, a relative MAE of 30% and a positive bias (0.04).

Overall, 30°-tilted cameras explain 87% spatial and temporal variations of LAI measured by LAI-2200 (Fig. 9b). The correspondence is further revealed by a low RMSE (0.73), a low MAE (0.52), and a low relative MAE (13%), considering the mean uncertainty of LAI-2200 measurements is up to (0.28, 7%). The discrepancies are mainly contributed by large LAI cases. When LAI > 6, the R^2, RMSE and MAE values are 0.11, 1.40, and 1.16, respectively. When LAI ⩽ 6, the R^2, RMSE and MAE values are 0.89, 0.52, and 0.40, respectively. This is probably because the estimation of LAI is highly sensitive to gap fractions in very dense canopy, in which case both image classification and LAI-2200 measurements are prone to uncertainties caused by multi-scattering effects.

Seasonal variations of LAI in four fields captured by the hand-held 30°-tilted cameras are all in line with LAI-2200, despite different seasonal trajectories (Fig. 10). In 2020, miscanthus LAI continuously increased until a high plateau above 6 in September, followed by a decreasing trend towards winter. Corn LAI reached a peak of 4 at the end of July and began to decrease gradually until harvest in October. A hailstorm hit the corn field on July 11 and ceased corn growth for several days. The two soybean fields differed in both magnitude and phenology. At Energy Farm, soybean LAI increased to 4 in mid-August and remained stable until senescence began in mid-September. At US-Bo1, soybean grew quickly in July and reached a peak of about 6.5 in early August.

Cameras are also able to capture the seasonality of GAI that LAI-2200 is unable to achieve (Fig. 10). In the miscanthus field, yellow/brown tissues started to develop in mid-August when LAI was still increasing. The discrepancy between LAI and GAI became larger in mid-September as the temperature declined quickly. In November, miscanthus LAI was still above 4 but GAI was already close to 0. In the corn field, maturity began in late August when leaves turned to yellow quickly. At harvest, there were still substantial leaves on, but all of them were yellow. Soybean was different from corn. Once a soybean leaf turned to yellow completely, it dropped in several days. As a result, LAI and GAI were relatively more coupled with each other during the senescence period than corn. Both LAI and GAI derived 30°-tilted cameras are comparable to those from destructive LAI at US-Bo1 (Fig. 10d).

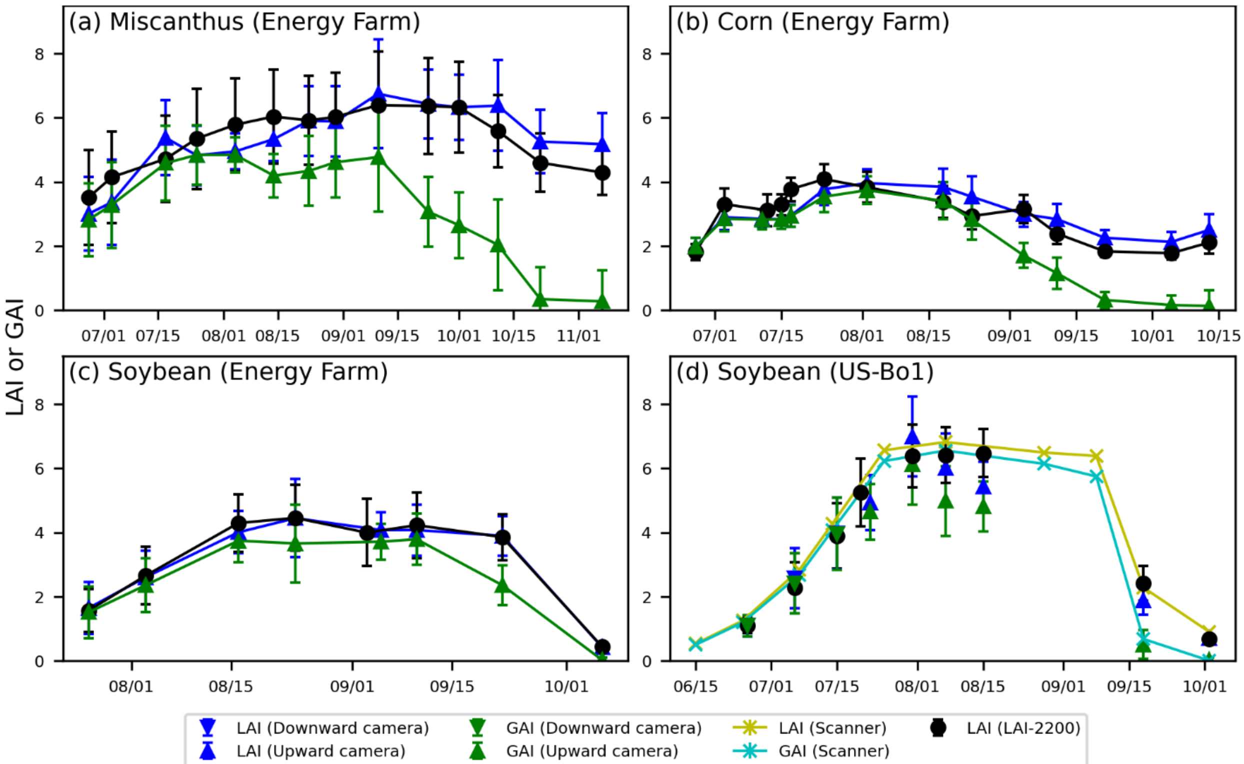

Fig. 10 Seasonal variation of LAI obtained from 30°-tilted hand-held cameras, LAI-2200, and destructive sampling in 2020. Each point is the average LAI from eight (Energy Farm) or 16 (US-Bo1) ESUs, and the error bar is the standard deviation over each ESU.

Validation for field-installed cameras

By deploying one downward viewing camera and eight upward viewing cameras in a 10 m × 10 m ESU in 2021 (Fig. 8), the acquired daily continuous corn LAI is almost the same as that acquired from manual LAI-2200 measurements (Fig. 11a and Fig. 12a), indicated by $R^2 = 0.98$, RMSE = 0.25 and MAE = 0.20 (7%). These errors are at the same level with the mean uncertainty of LAI-2200 measurements (0.26, 7%). Reducing the number of downward viewing cameras from eight to two can still maintain high accuracy. After testing all possible camera combinations, we found that using one camera placed at the position ¼ of the way between two rows observing in the direction along rows (A4) and another camera placed at the position of mid-row observing in the direction perpendicular to rows (B3) leads to the most similar LAI time series compared to using all eight (A1–B4) upward viewing cameras (Fig. 11a and Fig. 12b). Other camera combinations considering both along-rows and perpendicular-to-rows directions can also lead to reasonable performances, although the error statistics may double (Fig. 12c). In the soybean field, using one downward viewing camera and two upward viewing cameras (C2 and C4) leads to slightly lower accuracy than that in the corn field using the same camera combination (Fig. 11b and Fig. 12c), mainly because of higher LAI (>6) in soybean than in corn, which causes larger uncertainties in measurements.

Field-installed 30°-tilted cameras are also able to acquire daily continuous GAI (Fig. 11). In the corn field, GAI became slightly smaller than LAI since mid-July when entering the silking stage. The discrepancy became larger from September until the cameras were uninstalled due to an early harvest plan. In the soybean field, yellow leaves appeared in September, but the discrepancy between GAI and LAI was not large, because yellow leaves did not stay on plants for a long time. This is also revealed by destructive sampling.

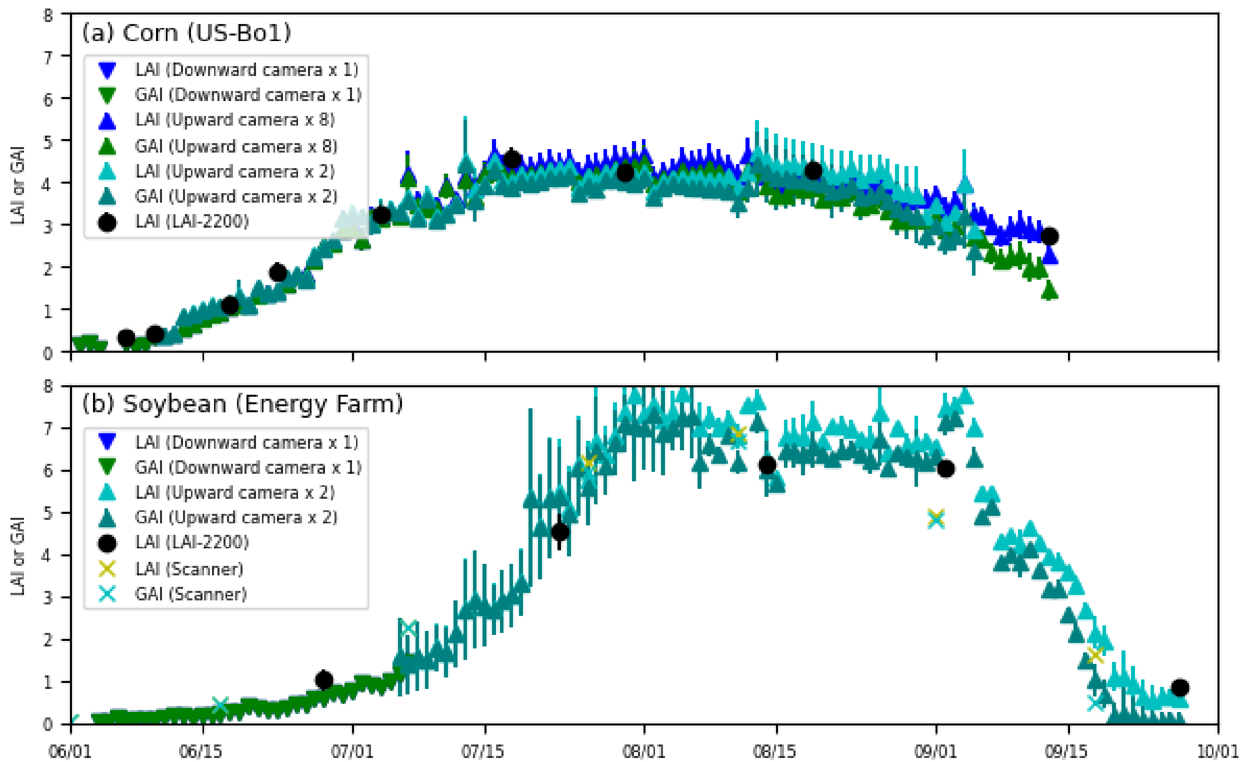

Fig. 11 Seasonal variation of LAI and GAI acquired by field-installed 30°-tilted cameras, LAI-2200, and destructive sampling in 2021.

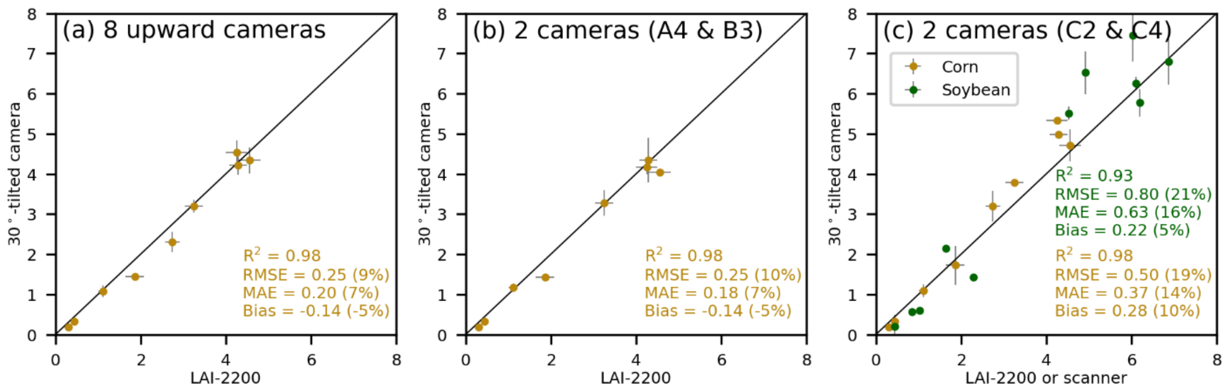

Fig. 12 Comparison of LAI acquired by field-installed 30°-tilted cameras with that acquired by LAI-2200 or destructive sampling.

LAI/GAI ground observation network

Fig. 13 shows daily continuous LAI and GAI data collected over six species at ten sites using 52 field-installed 30°-tilted cameras from May to November in 2022 (Table 1). Different LAI/GAI seasonal trajectories can be observed not only among different species but also within the same species. In general, corn and soybean had shorter peak growing seasons than other species, characterized by relatively sharp peaks between mid-July and mid-August. Corn 1 planted in early May reached peak about one month earlier than the other two corn fields which were planted in early June, but their senescence periods overlapped with each other with regards to both LAI and GAI. All three soybean fields reached peaks in mid-August, but their senescence periods were substantially different from each other. Miscanthus as a promising second-generation bioenergy crop had the latest peak time and highest peak value among all species. It continuously grew until mid-September, then LAI slowly decreased whereas GAI quickly decreased. Switchgrass as another second-generation bioenergy crop had similar LAI and GAI trends with miscanthus in early growing season. After reaching its peak in early July, its LAI and GAI became stable until senescence began in early September. Restored prairie had the earliest peak time and lowest LAI/GAI values among all species. They generally stayed stable from late June to late August. The deciduous forest site was not equipped with 30°-tilted cameras until mid-July. Since then, its LAI/GAI did not change during the peak growing season. It had the latest senescence among all species, and the senescence was the quickest: the GAI of the deciduous forest dropped from 4.8 to 0 within two weeks in October. The remaining forest LAI in November were woody components.

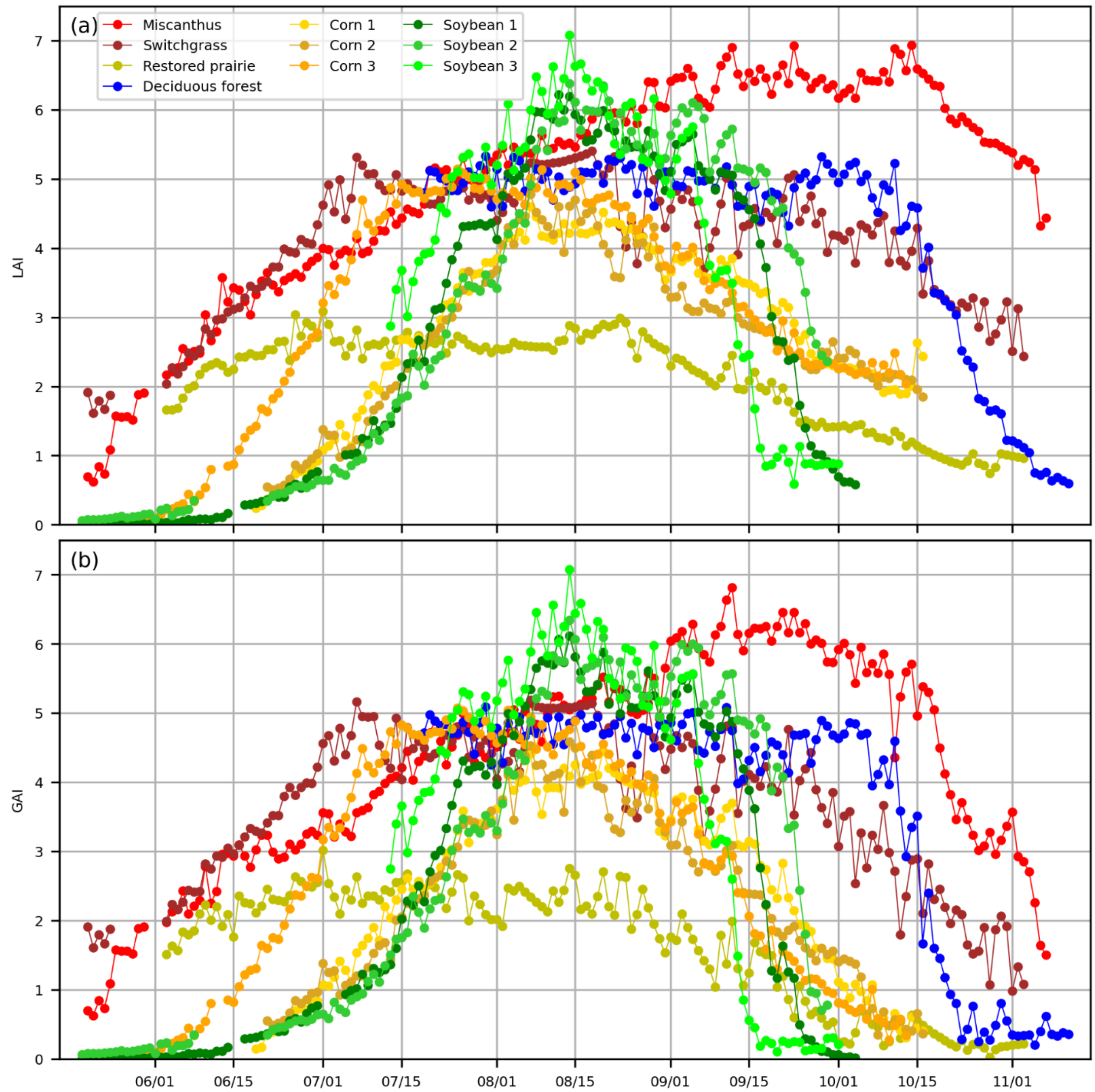

Fig. 13 Seasonal trajectories of (a) LAI and (b) GAI at ten sites acquired by field-installed 30°-tilted cameras in 2022. Downward viewing cameras were used until LAI reached 2, then upward viewing cameras were used.

Discussion

Efficacy of 30°-tilted cameras

The tilted camera method developed in this study takes advantages of directional and hemispherical cameras but avoid their disadvantages. The new method utilizes multi-angular gap fractions to constrain radiative transfer models as hemispherical cameras do and thus accurate and robust. It is easier to process thanks to full-frame usage, small geometric distortion, and constant and fine resolution, as directional cameras do. The key is that by tiling an ordinary camera a VZA range can be obtained on a per-pixel basis. We have proved it through both theoretical derivation and in-lab experiments (Fig. 2–5). Furthermore, compared to quantum sensors such as LAI-2200 and ceptometers, 30°-tilted cameras are superior in GAI quantification, less dependence on light conditions, and the avoidance of above-canopy and below-canopy measurement pair.

Other canopy structure variables, such as average leaf angle, apparent clumping index, diffuse non-interceptance, fraction of vegetation cover, and gap-size distribution can also be calculated as other instruments do. Although this study uses the same theory and implementation used by LAI-2200 to quantify LAI from 30°-tilted cameras, methods used by directional cameras, either 0° or 57.5°, and hemispherical cameras can also be applied to 30°-tilted cameras because the wide VZA range covered by 30°-tilted cameras. Moreover, tilting cameras by 30° is not mandatory. We chose 30° because at this tilting angle common cameras with FOV about 60–70° can cover all five VZA rings used by LAI-2200. Using the theoretical model (Eqn 8) and the polynomial model (Eqn 9), per-pixel VZA can be calculated for any tilting angle. The optimal choice of tilting angle may depend on the FOV of the used camera and the angles of interest for specific purposes.

The image classification algorithm developed in this study is generic and fully-automated. The innovations are two-fold. First, it unifies upward and downward viewing images by defining VIs which enhance the contrast between plant tissues and background while minimizing the within-class differences. Second, it uses an iterative peak detection strategy to deal with non-ideal histograms with more than or less than two peaks. The algorithm works well for all hand-held camera images and most of field-installed camera images, which ensures the efficient acquisition of spatially-distributed and temporally-continuous LAI/GAI data. Due to space limitation, we do not present analysis of failure cases here. A comprehensive evaluation of existing algorithms is still needed towards the development of a universal algorithm.

Uncertainties

The multi-scattering effect blurs pixels on the edges between vegetation and sky and causes unrealistic image classification. In this study, we only used images when light was diffuse and weak since strong beam light is the main cause of the multi-scattering effect (Bréda, 2003). Fortunately, this is intrinsically simple for field-installed cameras. We also tuned down relative exposure values for both hand-held and field-installed cameras to avoid overexposure (Chen et al., 1991). Big leaves and short canopies (0.5–3.5 m) in this study along with high resolution of cameras also ensure clear boundaries between vegetation and background on the captured images (Fig. 7). Mixed pixels are observable for the deciduous forest site with tall canopy. We envision that future field cameras with higher resolution, larger focal length or with RAW images can mitigate the mixed-pixel problem for forest applications (Hwang et al., 2016; Macfarlane et al., 2014).

Uncertainties specific to field-installed cameras included close leaves, water contamination and chromatic aberration. Crop leaves move from time to time, and close leaves could either block camera lens or disturb camera focus. Rain droplets or vapor condensation could blur images. In this study we visually selected high-quality images but we envision intellectual methods to be developed can improve the automation. Chromatic aberration of low-cost field cameras could cause difficulties in classifying green and non-green pixels. We envision that future field cameras with higher image quality and processing methods could solve the color problem for better GAI quantification. Finally, taking repetition by deploying more low-cost cameras is a simple option to reduce uncertainties.

Future opportunities

We have demonstrated that combining one downward viewing camera and two upward viewing cameras, the performance on LAI/GAI monitoring could be reasonably well for row crops. To date, there are many off-the-shelf field cameras with prices less than $100. This means with $200–300 one can acquire daily continuous LAI/GAI data at the ESU or plot level. Developing Internet-of-Things camera systems to automatically collect, process and transfer LAI/GAI data may further improve the feasibility of such a ground observation network at large scales. In addition, by using small camera modules, this method is promising to apply to mobile platforms such as tractors, robots, and drones. While existing studies have been using drone-mounted cameras to quantify LAI/GAI, they usually require ground truth data to train or calibrate models. By using our method, these are not required because this method is rooted from classic radiative transfer theory and is based on multi-angular gap fraction measurements. Besides automatic LAI/GAI data collection using field-installed cameras, this study also demonstrates the performance of manual LAI/GAI data collection by smartphone. Because the automatic VZA quantification and image classification algorithms developed in this study require very limited computational resources, it is promising to develop smartphone apps to achieve instant LAI/GAI quantification in the field, which can open a pathway to citizen science and complement the LAI/GAI ground observation network. The usage of ordinary cameras and simple algorithms which are available and accessible to anyone makes this new method highly feasible for broad applications.

The ultimate goal of developing the 30°-tilted camera method is to provide an accurate, robust, fully-automatic and standardized method for establishing a global LAI/GAI ground observation network. Through intensive validations for hand-held and filed-installed cameras, we have demonstrated the agreement between the new method and the standard commercial manually-operated instrument LAI-2200 on LAI measurements, and the consistency with the highly time-and-labor-intensive destructive sampling method on GAI measurements. By establishing a countywide ground observation network in six species including crops, tall grass and broadleaf forests, we have demonstrated the capability, generality, and scalability of using this new method to acquire spatially-distributed and temporally-continuous LAI and GAI data at the regional scale over the entire growing season. We believe this new method will substantially contribute to botanical, ecological, agricultural and remote sensing studies by filling the big field data gaps.

Acknowledgements

References

Baldocchi, D.: How Eddy Covariance Flux Measurements Have Contributed to Our Understanding of Global Change Biology, Glob. Chang. Biol., 1–19, https://doi.org/10.1111/gcb.14807, 2019.

Banan, D., Paul, R. E., Feldman, M. J., Holmes, M. W., Schlake, H., Baxter, I., Jiang, H., and Leakey, A. D. B.: High-fidelity detection of crop biomass quantitative trait loci from low-cost imaging in the field, 2, e00041, https://doi.org/10.1002/pld3.41, 2018.

Baret, F., de Solan, B., Lopez-Lozano, R., Ma, K., and Weiss, M.: GAI estimates of row crops from downward looking digital photos taken perpendicular to rows at 57.5° zenith angle: Theoretical considerations based on 3D architecture models and application to wheat crops, Agric. For. Meteorol., 150, 1393–1401, https://doi.org/10.1016/j.agrformet.2010.04.011, 2010.

Bréda, N. J. J.: Ground-based measurements of leaf area index: a review of methods, instruments and current controversies, J. Exp. Bot., 54, 2403–2417, https://doi.org/10.1093/JXB/ERG263, 2003.

Brede, B., Gastellu-Etchegorry, J. P., Lauret, N., Baret, F., Clevers, J. G. P. W., Verbesselt, J., and Herold, M.: Monitoring forest phenology and leaf area index with the autonomous, low-cost transmittance sensor PASTiS-57, Remote Sens., 10, 1032, https://doi.org/10.3390/rs10071032, 2018.

Brown, L. A., Ogutu, B. O., and Dash, J.: Tracking forest biophysical properties with automated digital repeat photography: A fisheye perspective using digital hemispherical photography from below the canopy, Agric. For. Meteorol., 287, 107944, https://doi.org/10.1016/j.agrformet.2020.107944, 2020.

Cescatti, A., Marcolla, B., Santhana Vannan, S. K., Pan, J. Y., Román, M. O., Yang, X., Ciais, P., Cook, R. B., Law, B. E., Matteucci, G., Migliavacca, M., Moors, E., Richardson, A. D., Seufert, G., and Schaaf, C. B.: Intercomparison of MODIS albedo retrievals and in situ measurements across the global FLUXNET network, Remote Sens. Environ., 121, 323–334, https://doi.org/10.1016/j.rse.2012.02.019, 2012.

Chen, J., Black, T. a., and Adams, R. S.: Evaluation of hemispherical photography for determining plant area index and geometry of a forest stand, Agric. For. Meteorol., 56, 129–143, https://doi.org/10.1016/0168-1923(91)90108-3, 1991.

Chen, J., Rich, P. M., Gower, S. T., Norman, J. M., and Plummer, S.: Leaf area index of boreal forests: Theory, techniques, and measurements, J. Geophys. Res., 102, 29429, https://doi.org/10.1029/97JD01107, 1997.

Demarez, V., Duthoit, S., Baret, F., Weiss, M., and Dedieu, G.: Estimation of leaf area and clumping indexes of crops with hemispherical photographs, Agric. For. Meteorol., 148, 644–655, https://doi.org/10.1016/j.agrformet.2007.11.015, 2008.

Dorigo, W. A., Wagner, W., Hohensinn, R., Hahn, S., Paulik, C., Xaver, A., Gruber, A., Drusch, M., Mecklenburg, S., Van Oevelen, P., Robock, A., and Jackson, T.: The International Soil Moisture Network: A data hosting facility for global in situ soil moisture measurements, Hydrol. Earth Syst. Sci., 15, 1675–1698, https://doi.org/10.5194/hess-15-1675-2011, 2011.

Fang, H.: Canopy clumping index (CI): A review of methods, characteristics, and applications, Agric. For. Meteorol., 303, https://doi.org/10.1016/j.agrformet.2021.108374, 2021.

Fang, H., Li, W., Wei, S., and Jiang, C.: Seasonal variation of leaf area index (LAI) over paddy rice fields in NE China: Intercomparison of destructive sampling, LAI-2200, digital hemispherical photography (DHP), and AccuPAR methods, Agric. For. Meteorol., 198–199, 126–141, https://doi.org/10.1016/j.agrformet.2014.08.005, 2014.

Fang, H., Ye, Y., Liu, W., Wei, S., and Ma, L.: Continuous estimation of canopy leaf area index (LAI) and clumping index over broadleaf crop fields: An investigation of the PASTIS-57 instrument and smartphone applications, Agric. For. Meteorol., 253–254, 48–61, https://doi.org/10.1016/j.agrformet.2018.02.003, 2018.

Fang, H., Baret, F., Plummer, S., and Schaepman-Strub, G.: An overview of global leaf area index (LAI): Methods, products, validation, and applications, Rev. Geophys., 2018RG000608, https://doi.org/10.1029/2018RG000608, 2019.

GCOS: The Global Observing System for Climate: Implementation Needs, 2016.

Gitelson, A. A. and Gamon, J. A.: The need for a common basis for defining light-use efficiency: Implications for productivity estimation, Remote Sens. Environ., 156, 196–201, https://doi.org/10.1016/j.rse.2014.09.017, 2015.

Hwang, Y., Ryu, Y., Kimm, H., Jiang, C., Lang, M., Macfarlane, C., and Sonnentag, O.: Correction for light scattering combined with sub-pixel classification improves estimation of gap fraction from digital cover photography, Agric. For. Meteorol., 222, 32–44, https://doi.org/10.1016/j.agrformet.2016.03.008, 2016.

Lang, A. R. G. and Xiang, Y.: Estimation of leaf area index from transmission of direct sunlight in discontinuous canopies, Agric. For. Meteorol., 37, 229–243, https://doi.org/10.1016/0168-1923(86)90033-X, 1986.

Leblanc, S. G., Chen, J. M., Fernandes, R., Deering, D. W., and Conley, A.: Methodology comparison for canopy structure parameters extraction from digital hemispherical photography in boreal forests, Agric. For. Meteorol., 129, 187–207, https://doi.org/10.1016/j.agrformet.2004.09.006, 2005.

Lecerf, R., Baret, F., Hanocq, J., Marloie, O., Rautiainen, M., Mottus, M., Heiskanen, J., and Stenberg, P.: PASTIS 57: Autonomous light sensors for PAI continuous monitoring. Principles, calibration and application to vegetation phenology, in: AGU Fall Meeting, 2010.

LI-COR: LAI-2200 Plant Canopy Analyzer: Instruction Manual, LI-COR Inc., Lincoln, Nebraska 60504, USA, 2021.

Li, K., Guan, K., Jiang, C., Wang, S., Peng, B., and Cai, Y.: Evaluation of Four New Land Surface Temperature (LST) Products in the U.S. Corn Belt: ECOSTRESS, GOES-R, Landsat, and Sentinel-3, IEEE J. Sel. Top. Appl. Earth Obs. Remote Sens., 14, 9931–9945, https://doi.org/10.1109/JSTARS.2021.3114613, 2021a.

Li, W. and Fang, H.: Estimation of direct, diffuse, and total FPARs from Landsat surface reflectance data and ground-based estimates over six FLUXNET sites, J. Geophys. Res. G Biogeosciences, 120, 96–112, https://doi.org/10.1002/2014JG002754, 2015.

Li, W., Fang, H., Wei, S., Weiss, M., and Baret, F.: Critical analysis of methods to estimate the fraction of absorbed or intercepted photosynthetically active radiation from ground measurements: Application to rice crops, Agric. For. Meteorol., 297, 108273, https://doi.org/10.1016/j.agrformet.2020.108273, 2021b.

Macfarlane, C.: Classification method of mixed pixels does not affect canopy metrics from digital images of forest overstorey, Agric. For. Meteorol., 151, 833–840, https://doi.org/10.1016/j.agrformet.2011.01.019, 2011.

Macfarlane, C., Hoffman, M., Eamus, D., Kerp, N., Higginson, S., McMurtrie, R., and Adams, M.: Estimation of leaf area index in eucalypt forest using digital photography, Agric. For. Meteorol., 143, 176–188, https://doi.org/10.1016/j.agrformet.2006.10.013, 2007.

Macfarlane, C., Ryu, Y., Ogden, G. N., and Sonnentag, O.: Digital canopy photography: Exposed and in the raw, Agric. For. Meteorol., 197, 244–253, https://doi.org/10.1016/j.agrformet.2014.05.014, 2014.

Miller, J. B.: A formula for average foliage density, Aust. J. Bot., 15, 141–144, https://doi.org/10.1071/BT9670141, 1967.

Monsi, M. and Saeki, T.: Uber den Lichtfaktor in den Pflanzen-gesellschaften und seine Bedeutung fur die Stoffproduktion, Jap. Journ. Bot., 14, 22–52, 1953.

Monsi, M. and Saeki, T.: On the factor light in plant communities and its importance for matter production, in: Annals of Botany, 549–567, https://doi.org/10.1093/aob/mci052, 2005.

Nilson, T.: A theoretical analysis of the frequencey of gaps in plant stands, Agric. Meteorlogy, 8, 25–38, https://doi.org/10.1016/0002-1571(71)90092-6, 1971.

Niu, X., Fan, J., Luo, R., Fu, W., Yuan, H., and Du, M.: Continuous estimation of leaf area index and the woody-to-total area ratio of two deciduous shrub canopies using fisheye webcams in a semiarid loessial region of China, Ecol. Indic., 125, 107549, https://doi.org/10.1016/j.ecolind.2021.107549, 2021.

Otsu, N.: A threshold selection method from gray-level histograms, IEEE Trans. Syst. Man. Cybern., 9, 62–66, 1979.

Qu, Y., Han, W., Fu, L., Li, C., Song, J., Zhou, H., Bo, Y., and Wang, J.: LAINet – A wireless sensor network for coniferous forest leaf area index measurement: Design, algorithm and validation, Comput. Electron. Agric., 108, 200–208, https://doi.org/10.1016/j.compag.2014.08.003, 2014.

Qu, Y., Wang, Z., Shang, J., Liu, J., and Zou, J.: Estimation of leaf area index using inclined smartphone camera, Comput. Electron. Agric., 191, 106514, https://doi.org/10.1016/j.compag.2021.106514, 2021.

Ridler, T. W. and Calvard, S.: PICTURE THRESHOLDING USING AN ITERATIVE SLECTION

METHOD., IEEE Trans. Syst. Man Cybern., SMC-8, 630–632, https://doi.org/10.1109/tsmc.1978.4310039, 1978.

Rosin, P. L.: Unimodal thresholding, Pattern Recognit., 34, 2083–2096, https://doi.org/10.1016/S0031-3203(00)00136-9, 2001.

Ryu, Y., Nilson, T., Kobayashi, H., Sonnentag, O., Law, B. E., and Baldocchi, D. D.: On the correct estimation of effective leaf area index: Does it reveal information on clumping effects?, Agric. For. Meteorol., 150, 463–472, https://doi.org/10.1016/j.agrformet.2010.01.009, 2010.

Ryu, Y., Verfaillie, J., Macfarlane, C., Kobayashi, H., Sonnentag, O., Vargas, R., Ma, S., and Baldocchi, D. D.: Continuous observation of tree leaf area index at ecosystem scale using upward-pointing digital cameras, Remote Sens. Environ., 126, 116–125, https://doi.org/10.1016/j.rse.2012.08.027, 2012.

Ryu, Y., Lee, G., Jeon, S., Song, Y., and Kimm, H.: Monitoring multi-layer canopy spring phenology of temperate deciduous and evergreen forests using low-cost spectral sensors, Remote Sens. Environ., 149, 227–238, https://doi.org/10.1016/j.rse.2014.04.015, 2014.

Schanda, J.: Colorimetry: Understanding the CIE System, 1–459 pp., https://doi.org/10.1002/9780470175637, 2007.

Sellers, P., Meeson, B., Hall, F., Asrar, G., Murphy, R., Schiffer, R., Bretherton, F., Dickinson, R., Ellingson, R., Field, C., Huemmrich, K., Justice, C., Melack, J., Roulet, N., Schimel, D., and Try, P.: Remote sensing of the land surface for studies of global change: Models — algorithms — experiments, Remote Sens. Environ., 51, 3–26, https://doi.org/10.1016/0034-4257(94)00061-Q, 1995.

Shih, Y., Lai, W. S., and Liang, C. K.: Distortion-free wide-angle portraits on camera phones, ACM Trans. Graph., 38, https://doi.org/10.1145/3306346.3322948, 2019.

Turner, D. P., Gower, S. T., Cohen, W. B., Gregory, M., and Maiersperger, T. K.: Effects of spatial variability in light use efficiency on satellite-based NPP monitoring, Remote Sens. Environ., 80, 397–405, https://doi.org/10.1016/S0034-4257(01)00319-4, 2002.

Wagner, S. and Hagemeier, M.: Method of segmentation affects leaf inclination angle estimation in hemispherical photography, Agric. For. Meteorol., 139, 12–24, https://doi.org/10.1016/j.agrformet.2006.05.008, 2006.

Wang, A., Zhang, W., and Wei, X.: A review on weed detection using ground-based machine vision and image processing techniques, Comput. Electron. Agric., 158, 226–240, https://doi.org/10.1016/j.compag.2019.02.005, 2019.

Wei, S., Yin, T., Dissegna, M. A., Whittle, A. J., Ow, G. L. F., Yusof, M. L. M., Lauret, N., and Gastellu-Etchegorry, J. P.: An assessment study of three indirect methods for estimating leaf area density and leaf area index of individual trees, Agric. For. Meteorol., 292–293, 108101, https://doi.org/10.1016/j.agrformet.2020.108101, 2020.

Welles, J. M. and Norman, J. M.: Instrument for Indirect Measurement of Canopy Architecture, Agron. J., 83, 818–825, https://doi.org/10.2134/agronj1991.00021962008300050009x, 1991.

White, M. a., Asner, G. P., Nemani, R. R., Privette, J. L., and Running, S. W.: Measuring fractional cover and leaf area index in arid ecosystems: Digital camera, radiation transmittance, and laser altimetry methods, Remote Sens. Environ., 74, 45–57, https://doi.org/10.1016/S0034-4257(00)00119-X, 2000.

Yan, G., Hu, R., Luo, J., Weiss, M., Jiang, H., Mu, X., Xie, D., and Zhang, W.: Review of indirect optical measurements of leaf area index: Recent advances, challenges, and perspectives, https://doi.org/10.1016/j.agrformet.2018.11.033, 2019.